Combining Bayesian reconstruction entropy with maximum entropy method for analytic continuations of matrix-valued Green's functions

Songlin Yang,[1] Liang Du,[1, *] and Li Huang[1, †]

[1]*College of Physics and Technology, Guangxi Normal University, Guilin, Guangxi 541004, China*
(Dated: January 2, 2024)

The Bayesian reconstruction entropy is considered an alternative to the Shannon-Jaynes entropy, as it does not exhibit the asymptotic flatness characteristic of the Shannon-Jaynes entropy and obeys the scale invariance. It is commonly utilized in conjunction with the maximum entropy method to derive spectral functions from Euclidean time correlators produced by lattice QCD simulations. This study expands the application of the Bayesian reconstruction entropy to the reconstruction of spectral functions for Matsubara or imaginary-time Green's functions in quantum many-body physics. Furthermore, it extends the Bayesian reconstruction entropy to implement the positive-negative entropy algorithm, enabling the analytic continuations of matrix-valued Green's functions on an element-wise manner. Both the diagonal and off-diagonal components of the matrix-valued Green's functions are treated equally. Benchmark results for the analytic continuations of synthetic Green's functions indicate that the Bayesian reconstruction entropy, when combined with the preblur trick, demonstrates comparable performance to the Shannon-Jaynes entropy. Notably, it exhibits greater resilience to noises in the input data, particularly when the noise level is moderate.

I. INTRODUCTION

In quantum many-body physics, single-particle Green's function holds significant importance [1, 2]. It is typically computed using numerical methods such as quantum Monte Carlo [3–5] and functional renormalization group [6, 7], or many-body perturbative techniques like random phase approximation [8, 9] and GW approximation [10–13], within the framework of imaginary time or Matsubara frequency formulation. This quantity provides valuable insights into the dynamic response of the system. However, it cannot be directly compared to real-frequency experimental observables. Therefore, it is necessary to convert the calculated values to real frequencies, which presents the fundamental challenge of the analytic continuation problem. In theory, the retarded Green's function $G^R(\omega)$ and the spectral function $A(\omega)$ can be derived from the imaginary-time Green's function $G(\tau)$ or Matsubara Green's function $G(i\omega_n)$ by performing an inverse Laplace transformation [1, 2]. Due to the ill-conditioned nature of the transformation kernel, solving it directly is nearly impossible. In fact, the output for this inverse problem is highly sensitive to the input. Even minor fluctuations or noises in $G(\tau)$ or $G(i\omega_n)$ can result in nonsensical changes for $A(\omega)$ or $G^R(\omega)$, making analytic continuations extremely unstable.

In recent decades, numerous techniques have been developed to address the challenges associated with analytic continuation problems. These methods include Padé approximation (PA) [14–17], maximum entropy method (MaxEnt) [18–20], stochastic analytic continuation (SAC) [21–30], stochastic optimization method (SOM) [31–35], stochastic pole expansion (SPX) [36, 37], sparse modeling (SpM) [38, 39], Nevanlinna analytical continuation (NAC) [40, 41], causal projections [42], Prony fits [43–45], and machine learning assistant approaches [46–52], and so on. Each method has

its own advantages and disadvantages. There is no doubt that the MaxEnt method is particularly popular due to its ability to maintain a balance between computational efficiency and accuracy [18–20]. Several open source toolkits, such as ΩMAXENT [53], QMEM [54], MAXENT by Kraberger *et al.* [55], MAXENT by Levy *et al.* [56], ALF [57], ACFlow [58], eDMFT [59], and ana_cont [60], have been developed to implement this method.

The MaxEnt method is rooted in Bayesian inference [61]. Initially, the spectral function $A(\omega)$ is constrained to be non-negative and is interpreted as a probability distribution. Subsequently, the MaxEnt method endeavors to identify the most probable spectrum by minimizing a functional $Q[A]$, which comprises the misfit functional $L[A]$ and the entropic term $S[A]$ [see Eq. (10)]. Here, $L[A]$ quantifies the difference between the input and reconstructed Green's function, while $S[A]$ is employed to regulate the spectrum [18]. The MaxEnt method is well-established for the diagonal components of matrix-valued Green's functions, as the corresponding spectral functions are non-negative (for fermionic systems). However, the non-negativity of the spectral functions cannot be assured for the off-diagonal components of matrix-valued Green's functions. As a result, conventional MaxEnt method fails in this situation.

Currently, there is a growing emphasis on obtaining the full matrix representation of the Green's function (or the corresponding self-energy function) on the real axis [54, 62]. This is necessary for calculating lattice quantities of interest in Dyson's equation [59]. Therefore, there is a strong demand for a reliable method to perform analytic continuation of the entire Green's function matrix [41–43]. To meet this requirement, several novel approaches have been suggested in recent years as enhancements to the conventional MaxEnt method. The three most significant advancements are as follows: (1) *Auxiliary Green's function algorithm*. It is possible to create an auxiliary Green's function by combining the off-diagonal and diagonal elements of the matrix-valued Green's function to ensure the positivity of the auxiliary spectrum [63–68]. The analytic continuation of the auxiliary Green's function can

then be carried out using the standard MaxEnt method. (2) *Positive-negative entropy algorithm*. Kraberger *et al.* proposed that the off-diagonal spectral functions can be seen as a subtraction of two artificial positive functions. They extended the entropic term to relax the non-negativity constraint presented in the standard MaxEnt method [55, 60]. This enables simultaneous treatment of both the diagonal and off-diagonal elements, thereby restoring crucial constraints on the mathematical properties of the resulting spectral functions, including positive semi-definiteness and Hermiticity. (3) *Maximum quantum entropy algorithm*. Recently, Sim and Han generalized the MaxEnt method by reformulating it with quantum relative entropy, maintaining the Bayesian probabilistic interpretation [18, 61]. The matrix-valued Green's function is directly continued as a single object without any further approximation or ad-hoc treatment [54].

Although various algorithms have been proposed to enhance the usefulness of the MaxEnt method [53–55], further improvements in algorithms and implementations are always beneficial. As mentioned above, the essence of the MaxEnt method lies in the definition of the entropic term $S[A]$. Typically, it takes the form of Shannon-Jaynes entropy (dubbed S_{SJ}) in the realm of quantum many-body physics [69]. However, alternative forms such as the Tikhonov regulator [70], the positive-negative entropy [55], and the quantum relative entropy [54] are also acceptable. It is worth noting that in the context of lattice QCD simulations, the extraction of spectral functions from Euclidean time correlators is of particular important. The MaxEnt method is also the primary tool for the analytic continuation of lattice QCD data [71]. Burnier and Rothkopf introduced an enhanced dimensionless prior distribution, known as the Bayesian reconstruction entropy (dubbed S_{BR}) [72, 73], which demonstrates superior asymptotic behavior compared to S_{SJ} [69]. They discovered that by using S_{BR} in conjunction with the MaxEnt method, a significant improvement in the reconstruction of spectral functions for Euclidean time correlators can be achieved. They latter extended S_{BR} to support Bayesian inference of non-positive spectral functions in quantum field theory [74]. But to the best of our knowledge, the application of S_{BR} has been limited to postprocessing for lattice QCD data thus far. Hence, some questions naturally arise. How effective is S_{BR} for solving analytic continuation problems in quantum many-body simulations? Is it truly superior to S_{SJ}? Keeping these questions in mind, the primary objective of this study is to broaden the application scope of S_{BR}. We at first verify whether S_{BR} can handle Matsubara (or imaginary-time) Green's functions. Then, we generalize S_{BR} to implement the positive-negative entropy algorithm [55] for analytic continuations of matrix-valued Green's functions. The simulated results indicate that S_{BR} works quite well in transforming imaginary-time or Matsubara Green's function data to real frequency, no matter whether the Green's function is a matrix or not. We find that S_{BR} has a tendency to sharpen the peaks in spectral functions, but this shortcoming can be largely overcame by the preblur trick [55, 60]. Overall, the performance of S_{BR} is comparable to that of S_{SJ} [69] for the examples involved.

The rest of this paper is organized as follows. Section II

introduces the spectral representation of the single-particle Green's function. Furthermore, it explains the fundamental formalisms of the MaxEnt method, the Bayesian reconstruction entropy, and the principle of the positive-negative entropy algorithm. Section III is dedicated to various benchmark examples, including analytic continuation results for synthetic single-band Green's functions and multi-orbital matrix-valued Green's functions. The spectral functions obtained by S_{SJ} and S_{BR} are compared with the exact spectra. In Section IV, we further examine the preblur trick and the auxiliary Green's function algorithm for S_{SJ} and S_{BR}. The robustness of S_{BR} with respect to noisy Matsubara data is discussed and compared with that of S_{SJ}. A concise summary is presented in Section V. Finally, Appendix A introduces the goodness-of-fit functional. The detailed mathematical derivations for S_{SJ} and S_{BR} are provided in Appendices B and C, respectively.

II. METHOD

A. Spectral representation of single-particle Green's function

It is well known that the single-particle imaginary-time Green's function $G(\tau)$ can be defined as follows:

$$G(\tau) = \langle \mathcal{T}_\tau d(\tau) d^\dagger(0) \rangle, \tag{1}$$

where τ is imaginary time, $\mathcal{T}_\tau$ means the time-ordered operator, d ($d^\dagger$) denotes the annihilation (creation) operator [1, 2]. Given $G(\tau)$, Matsubara Green's function $G(i\omega_n)$ can be constructed via direct Fourier transformation:

$$G(i\omega_n) = \int_0^\beta d\tau\, e^{-i\omega_n\tau} G(\tau), \tag{2}$$

where β is the inverse temperature of the system ($\beta \equiv 1/T$), and ω_n is the Matsubara frequency. Note that ω_n is equal to $(2n+1)\pi/\beta$ for fermions and $2n\pi/\beta$ for bosons (n is an integer).

Let us assume that the spectral function of the single-particle Green's function is $A(\omega)$, then the spectral representations of $G(\tau)$ and $G(i\omega_n)$ read:

$$G(\tau) = \int_{-\infty}^{+\infty} K(\tau, \omega) A(\omega) d\omega, \tag{3}$$

and

$$G(i\omega_n) = \int_{-\infty}^{+\infty} K(i\omega_n, \omega) A(\omega) d\omega, \tag{4}$$

respectively. Here, $K(\tau, \omega)$ and $K(i\omega_n, \omega)$ are called the kernel functions. Their definitions are as follows:

$$K(\tau, \omega) = \frac{e^{-\tau\omega}}{1 \pm e^{-\beta\omega}}, \tag{5}$$

and

$$K(i\omega_n, \omega) = \frac{1}{i\omega_n - \omega}. \tag{6}$$

In the right-hand side of Eq. (5), + is for fermionic correlators and - is for bosonic correlators [18]. In the subsequent discussion, our focus will be on fermionic correlators.

We observe that Eqs. (3) and (4) are classified as Fredholm integral equations of the first kind. When $A(\omega)$ is given, it is relatively straightforward to compute the corresponding $G(\tau)$ and $G(i\omega_n)$ by numerical integration methods. However, the inverse problem of deducing $A(\omega)$ from $G(\tau)$ or $G(i\omega_n)$ is challenging due to the ill-conditioned nature of the kernel function K. To be more specific, the condition number of K is very large because of the exponential decay of K with ω and τ. Consequently, direct inversion of K becomes impractical from a numerical standpoint [19]. Furthermore, the $G(\tau)$ or $G(i\omega_n)$ data obtained from finite temperature quantum Monte Carlo simulations is not free from errors [3–5], further complicating the solution of Eqs. (3) and (4).

B. Maximum entropy method

The cornerstone of the MaxEnt method is Bayes' theorem. Let us treat the input Green's function G and the spectrum A as two events. According to Bayes' theorem, the posterior probability $P[A|G]$ can be calculated by:

$$P[A|G] = \frac{P[G|A]P[A]}{P[G]}, \tag{7}$$

where $P[G|A]$ is the likelihood function, $P[A]$ is the prior probability, and $P[G]$ is the evidence [61]. $P[G|A]$ is assumed to be in direct proportion to $e^{-L[A]}$, where the misfit functional $L[A]$ reads:

$$L[A] = \frac{1}{2}\chi^2[A] = \frac{1}{2}\sum_{i=1}^{N}\left(\frac{G_i - \tilde{G}_i[A]}{\sigma_i}\right)^2. \tag{8}$$

Here, N is the number of input data points, σ denotes the standard deviation of G, $\tilde{G}[A]$ is the reconstructed Green's function via Eqs. (3) and (4), and $\chi^2[A]$ is called the goodness-of-fit functional (see Appendix A for more details). On the other hand, $P[A]$ is supposed to be in direct proportion to $e^{\alpha S[A]}$, where α is a regulation parameter and S is entropy. Since the evidence $P[G]$ can be viewed as a normalization constant, it is ignored in what follows. Thus,

$$P[A|G] \propto e^{Q}, \tag{9}$$

where Q is a functional of A [18]. It is defined as follows:

$$Q[A] = \alpha S[A] - L[A] = \alpha S[A] - \frac{1}{2}\chi^2[A]. \tag{10}$$

The basic idea of the MaxEnt method is to identify the optimal spectrum $\hat{A}$ that maximizes the posterior probability $P[A|G]$ (or equivalently $Q[A]$). In essence, our goal is to determine the most favorable $\hat{A}$ that satisfies the following equation:

$$\left.\frac{\partial Q}{\partial A}\right|_{A=\hat{A}} = 0. \tag{11}$$

Eq. (11) can be easily solved by the standard Newton's algorithm [75]. In Appendices A, B and C, all terms in the right-hand side of Eq. (10) are elaborated in detail. We also explain how to solve Eq. (11) efficiently.

C. Bayesian reconstruction entropy

The entropy S is also known as the Kullback-Leibler distance sometimes. In principle, there are multiple choices for it. Perhaps S_{SJ} is the most frequently used in quantum many-body physics and condensed matter physics [18, 69]. It reads:

$$S_{\text{SJ}}[A] = \int d\omega \left[A(\omega) - D(\omega) - A(\omega)\log\left(\frac{A(\omega)}{D(\omega)}\right)\right]. \tag{12}$$

Here, $D(\omega)$ is called the default model, providing the essential features of spectra. Usually $D(\omega)$ is a constant or a Gaussian function, but it can be determined by making use of high-frequency behavior of input data as well [53]. If both $A(\omega)$ and $D(\omega)$ have the same normalization, Eq. (12) reduces to:

$$S_{\text{SJ}}[A] = -\int d\omega\, A(\omega)\log\left(\frac{A(\omega)}{D(\omega)}\right). \tag{13}$$

The S_{BR} introduced by Burnier and Rothkopf [72, 73] is dominant in high-energy physics and particle physics. It reads:

$$S_{\text{BR}}[A] = \int d\omega \left[1 - \frac{A(\omega)}{D(\omega)} + \log\left(\frac{A(\omega)}{D(\omega)}\right)\right]. \tag{14}$$

Note that S_{SJ} is constructed from four axioms [18]. While for S_{BR}, two of these axioms are replaced [72]. First of all, the scale invariance is incorporated in S_{BR}. It means that S_{BR} only depends on the ratio between A and D. The integrand in Eq. (14) is dimensionless, such that the choice of units for A and D will not change the result of the spectral reconstruction. Second, S_{BR} favors choosing smooth spectrum. The spectra that deviate between two adjacent frequencies, ω_1 and ω_2, should be penalized.

D. Positive-negative entropy

The formulas discussed above are only correct for positive definite spectra with a finite norm, i.e.,

$$\int d\omega\, A(\omega) > 0. \tag{15}$$

However, the norm could be zero for off-diagonal elements of matrix-valued Green's functions due to the fermionic anti-commutation relation [1, 42]:

$$\int d\omega\, A(\omega) = 0. \tag{16}$$

This suggests that the spectral function is not positive definite any more. The equations for S_{SJ} and S_{BR} [i.e., Eqs. (12) and (14)] should be adapted to this new circumstance. The positive-negative entropy algorithm proposed by Kraberger *et al.* is a graceful solution to this problem [55, 60]. They rewrite the off-diagonal spectral function $A(\omega)$ as the subtraction of two positive definite spectra:

$$A(\omega) = A^{+}(\omega) - A^{-}(\omega). \tag{17}$$

Here $A^+(\omega)$ and $A^-(\omega)$ are independent, but have the same norm. Then the resulting entropy can be split into two parts:

$$S^{\pm}[A] = S[A^+, A^-] = S[A^+] + S[A^-]. \quad (18)$$

$S^{\pm}[A]$ (or $S[A^+, A^-]$) is called the positive-negative entropy, which was first used for the analysis of NMR spectra [76, 77]. The expressions of positive-negative entropy for S_{SJ} and S_{BR} are as follows:

$$S^{\pm}_{SJ}[A] = \int d\omega \left[\sqrt{A^2 + 4D^2} - 2D - A \log\left(\frac{\sqrt{A^2 + 4D^2} + A}{2D} \right) \right], \quad (19)$$

and

$$S^{\pm}_{BR}[A] = \int d\omega \left[2 - \frac{\sqrt{A^2 + D^2} + D}{D} + \log\left(\frac{\sqrt{A^2 + D^2} + D}{2D} \right) \right]. \quad (20)$$

$$s_{BR}(x) = 1 - x + \log x, \quad (23)$$

$$s^{\pm}_{SJ}(x) = \sqrt{x^2 + 4} - 2 - x \log \frac{\sqrt{x^2 + 4} + x}{2}, \quad (24)$$

$$s^{\pm}_{BR}(x) = 2 - (\sqrt{x^2 + 1} + 1) + \log \frac{\sqrt{x^2 + 1} + 1}{2}. \quad (25)$$

They are visualized in Figure 1.

Clearly, all the entropy densities are strictly convex and non-positive (i.e., $s \leq 0$ and $s^{\pm} \leq 0$). The ordinary entropy density $s(x)$ is just defined for positive x. $s_{BR}(x)$ becomes maximal at $x = 1$, and exhibits a similar quadratic behavior around its maximum as $s_{SJ}(x)$. In the case $x \to 0$ ($A \ll D$), $s_{BR}(x)$ is not suppressed, while $s_{SJ}(x) \to -1$. Thus, $s_{BR}(x)$ avoids the asymptotic flatness inherent in $s_{SJ}(x)$ [72]. The positive-negative entropy density $s^{\pm}(x)$ is valid for any x ($x \in \mathbb{R}$). Both $s^{\pm}_{BR}(x)$ and $s^{\pm}_{SJ}(x)$ are even functions. They also exhibit quadratic behaviors around $x = 0$, and $s^{\pm}_{BR}(x) \geq s^{\pm}_{SJ}(x)$. In the limit of $\alpha \to \infty$, the goodness-of-fit functional $\chi^2[A]$ has negligible weight, and the entropic term $\alpha S[A]$ becomes dominant [53]. Thus, the maximization of $Q[A]$ (equivalently, the maximization of $S[A]$) yields $\hat{A} = D$ (at $x = 1$) for conventional entropy, in contrast to $\hat{A} = 0$ (at $x = 0$) for the positive-negative entropy [55].

FIG. 1. Comparison of entropy densities for different entropic terms. The entropy S is related to the entropy density s via Eq. (21). For the positive-negative entropy $S^{\pm}$, $D^+ = D^- = D$ is assumed.

The default models for A^+ and A^- are D^+ and D^-, respectively. To derive Eqs. (19) and (20), $D^+ = D^- = D$ is assumed. For a detailed derivation, please see Appendices B and C. Similar to $S_{BR}[A]$, $S^{\pm}_{BR}[A]$ also exhibits scale invariance. In other words, it depends on A/D only.

E. Entropy density

The integrand in the expression for entropy S is referred as entropy density s, i.e.,

$$S[A] = \int d\omega \, s[A(\omega)]. \quad (21)$$

Next, we would like to make a detailed comparison about the entropy densities of different entropic terms. Supposed that $x = A/D$, the expressions for various entropy densities are collected as follows:

$$s_{SJ}(x) = x - 1 - x \log x, \quad (22)$$

III. RESULTS

A. Computational setups

When the conventional MaxEnt method is combined with S_{SJ} (or $S^{\pm}_{SJ}$) [69], it is called the MaxEnt-SJ method. On the other hand, a combination of the MaxEnt method with S_{BR} (or $S^{\pm}_{BR}$) [72–74] is called the MaxEnt-BR method. We implemented both methods in the open source analytic continuation toolkit, namely ACFlow [58]. All the benchmark calculations involved in this paper were done by this toolkit. The simulated results for the MaxEnt-SJ and MaxEnt-BR methods will be presented in this section. Next, we will explain the computational details.
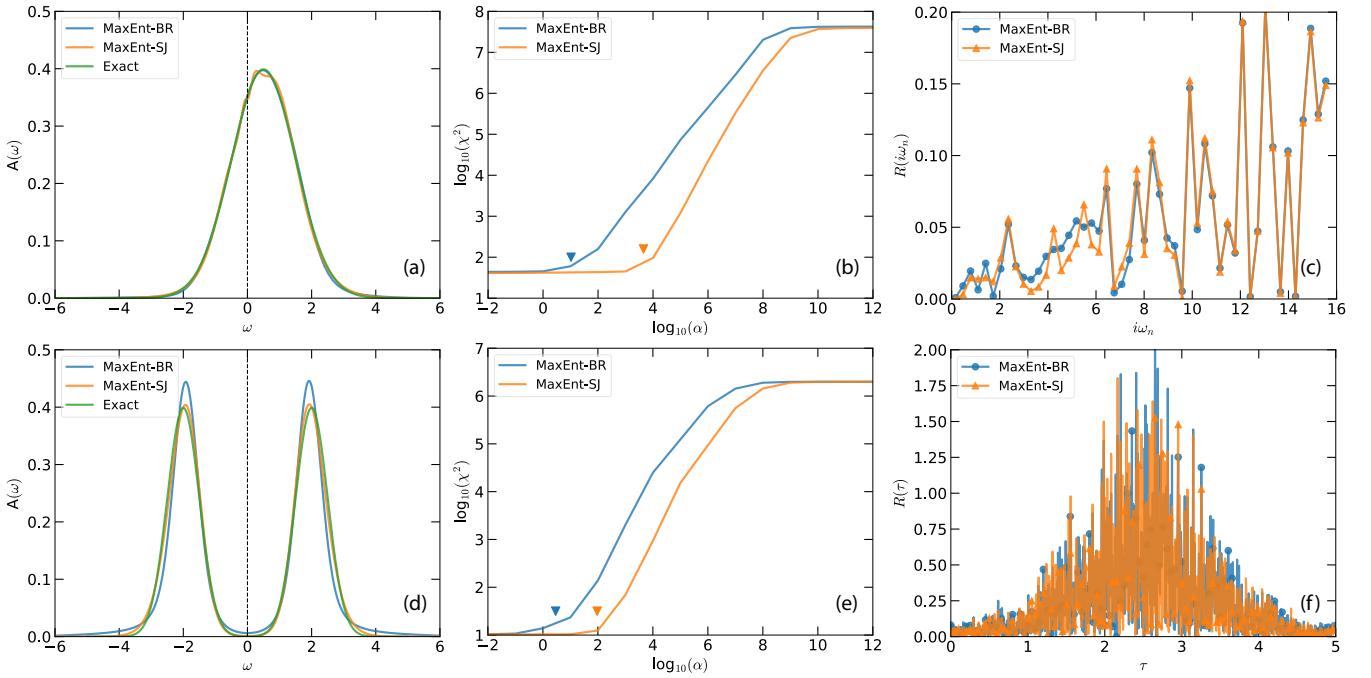
FIG. 2. Analytic continuations of single-band Green's functions. (a)-(c) For single off-centered peak case. (d)-(f) For two Gaussian peaks with a gap case. In panels (a) and (d), the calculated and exact spectra are compared. In panels (b) and (e), the $\log_{10}(\chi^2) - \log_{10}(\alpha)$ curves are plotted. The inverted triangle symbols indicate the optimal α parameters, which are determined by the χ^2-kink algorithm [53]. The deviations of the reproduced Green's function from the raw ones are shown in panels (c) and (f). Note that in panel (c), R is a function of Matsubara frequency. However, R is τ-dependent in panel (c).

We always start from an exact spectrum $A(\omega)$, which consists of one or more Gaussian-like peaks. Then $A(\omega)$ is used to construct the imaginary-time Green's function $G(\tau)$ via Eq. (3), or the Matsubara Green's function $G(i\omega_n)$ via Eq. (4). Here, for the sake of simplicity, the kernel function K is assumed to be fermionic. Since the realistic Green's function data from finite temperature quantum Monte Carlo simulations is usually noisy, multiplicative Gaussian noise will be manually added to the clean $G(\tau)$ or $G(i\omega_n)$ to imitate this situation. The following formula is adopted:

$$G_{\text{noisy}} = G_{\text{clean}}[1 + \delta N_{\mathbb{C}}(0, 1)], \qquad (26)$$

where δ denotes the noise level of the input data and $N_{\mathbb{C}}$ is the complex-valued normal Gaussian noise [42]. Unless stated otherwise, the standard deviation of G is fixed to 10^{-4}. The numbers of input data for $G(\tau)$ and $G(i\omega_n)$ are 1000 and 50, respectively. During the MaxEnt simulations, the χ^2-kink algorithm [53] is used to determine the regulation parameter α. The Bryan algorithm [78] is also tested. It always gives similar results, which will not be presented in this paper. Once S_{BR} and $S_{\text{BR}}^{\pm}$ are chosen, the preblur trick [55, 60] is used to smooth the spectra. The blur parameter is adjusted case by case. Finally, the reconstructed spectrum is compared with the true solution. We also adopt the following quantity to quantify the deviation of the reconstructed Green's function from the input one:

$$R_i = 100 \left| \frac{\Delta G_i}{G_i} \right| = 100 \left| \frac{G_i - \tilde{G}_i[\hat{A}]}{G_i} \right|, \qquad (27)$$

where $\tilde{G}$ is evaluated by $\hat{A}$ via Eq. (3) or Eq. (4).

B. Single-band Green's functions

At first, the analytic continuations of single-band Green's functions are examined. The exact spectral functions are constructed by a superposition of some Gaussian peaks. We consider two representative spectra. (i) Single off-centered peak. The spectral function is:

$$A(\omega) = \exp\left[-\frac{(\omega - \epsilon)^2}{2\Gamma^2} \right], \qquad (28)$$

where $\epsilon = 0.5$, $\Gamma = 1.0$, $\delta = 10^{-4}$, $\sigma = 10^{-4}$, and $\beta = 20.0$. The input data is Matsubara Green's function, which contains 50 Matsubara frequencies ($N = 50$). The blur parameter for the MaxEnt-BR method is 0.45. (ii) Two Gaussian peaks with a gap. The spectral function is:

$$\begin{aligned} A(\omega) &= \frac{f_1}{\sqrt{2\pi}\Gamma_1} \exp\left[-\frac{(\omega - \epsilon_1)^2}{2\Gamma_1^2} \right] \\ &+ \frac{f_2}{\sqrt{2\pi}\Gamma_2} \exp\left[-\frac{(\omega - \epsilon_2)^2}{2\Gamma_2^2} \right], \end{aligned} \qquad (29)$$

where $f_1 = f_2 = 1.0$, $\epsilon_1 = -\epsilon_2 = 2.0$, $\Gamma_1 = \Gamma_2 = 0.5$, $\delta = 10^{-4}$, $\sigma = 10^{-3}$, and $\beta = 5.0$. The synthetic data is imaginary-time Green's function, which contains 1000 imaginary time slices
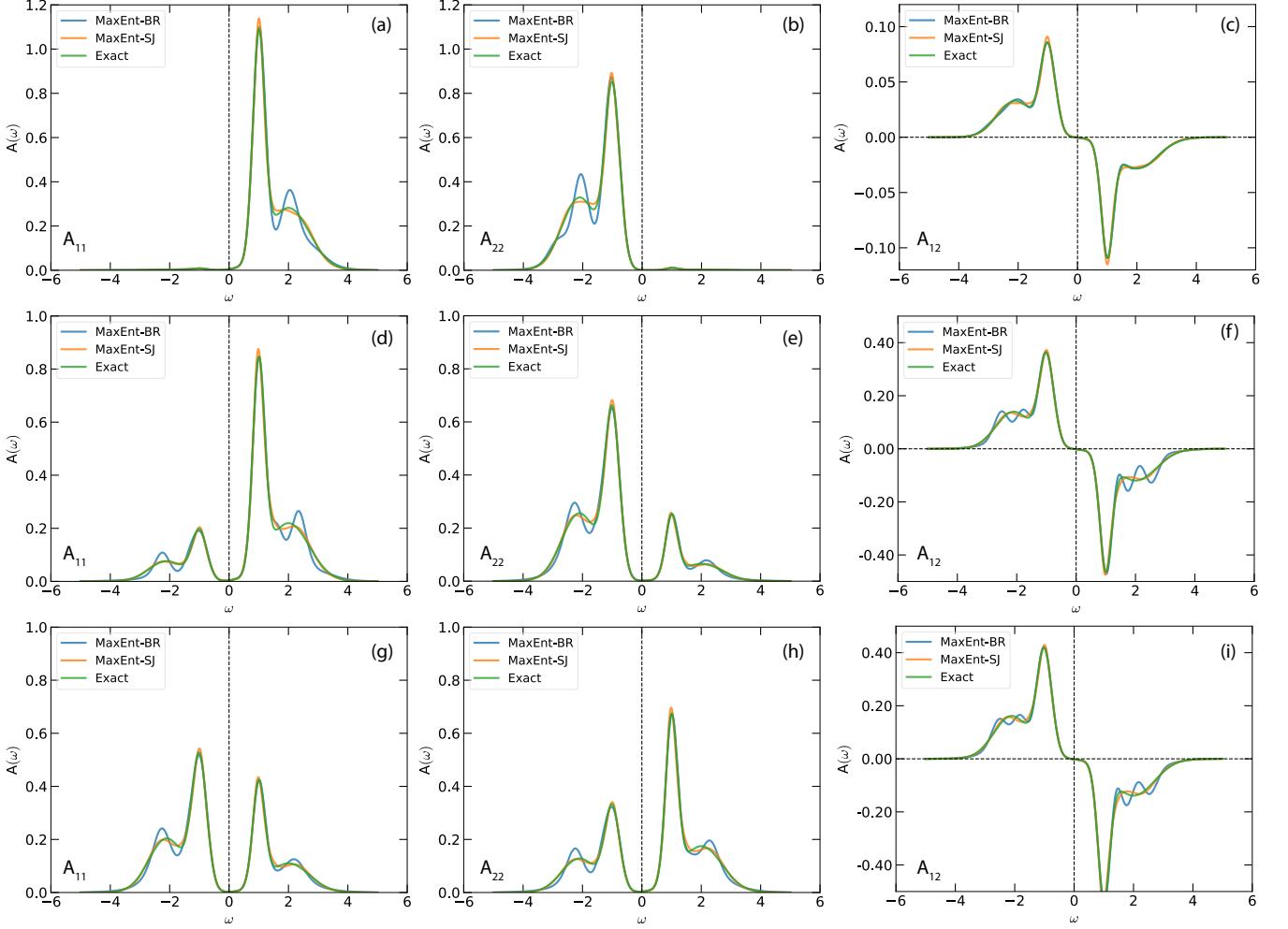
FIG. 3. Analytic continuations of two-band matrix-valued Green's functions. For analytic continuations for the diagonal elements of the Green's function, S_{SJ} and S_{BR} are used in the calculations. While for the off-diagonal elements of the Green's functions, $S_{SJ}^{\pm}$ and $S_{BR}^{\pm}$ are employed. In the MaxEnt-BR simulations, the preblur trick is always applied, and the blur parameter b is fixed to 0.2. The default models for off-diagonal calculations are constructed by A_{11} and A_{22}. See main text for more details. (a)-(c) $\theta = 0.1$; (d)-(f) $\theta = 0.5$; (g)-(i) $\theta = 0.9$.

($N = 1000$). The blur parameter for the MaxEnt-BR method is 0.30.

The analytic continuation results are shown in Fig. 2. For case (i), it is clear that the exact spectrum and Matsubara Green's function are well reproduced by both the MaxEnt-SJ method and the MaxEnt-BR method [see Fig. 2(a) and (c)]. For case (ii), the MaxEnt-SJ method works quite well. The MaxEnt-BR method can resolve the gap and the positions of the two peaks accurately. However, it slightly overestimates their heights. We also observe that the difference between $G(\tau)$ and $\tilde{G}(\tau)$ becomes relatively apparent in the vicinity of $\tau = \beta/2$ [see Fig. 2(d) and (f)]. Figure 2(b) and (e) plot $\log_{10}(\chi^2)$ as a function of $\log_{10}(\alpha)$. The plots can be split into three distinct regions [53]: (i) *Default model region* ($\alpha \to \infty$). χ^2 is relatively flat and goes to its global maximum. The entropic term αS is much larger than χ^2. The obtained spectrum $A(\omega)$ resembles the default model $D(\omega)$. (ii) *Noise-fitting region* ($\alpha \to 0$). χ^2 approaches its global minimum, but it is larger than αS. In this region, the calculated spectrum $A(\omega)$

tends to fit the noise in $G(\tau)$ or $G(i\omega_n)$. (iii) *Information-fitting region*. χ^2 increases with the increment of α. It is comparable with αS. The optimal α parameter is located at the crossover between the noise-fitting region and the information-fitting region. For S_{BR} and S_{SJ}, their $\chi^2(\alpha)$ curves almost overlap at the default model region and the noise-fitting region, but differ at the information-fitting region. It indicates that the optimal α parameters for S_{SJ} are larger than those for S_{BR}.

C. Matrix-valued Green's functions

Next, the analytic continuations of matrix-valued Green's functions are examined. We consider a two-band model. The initial spectral function is a diagonal matrix:

$$\mathbf{A}'(\omega) = \begin{bmatrix} A'_{11}(\omega) & 0 \\ 0 & A'_{22}(\omega) \end{bmatrix}. \tag{30}$$

Here $A'_{11}(\omega)$ and $A'_{22}(\omega)$ are constructed by using Eq. (29). For $A'_{11}(\omega)$, the parameters are: $f_1 = f_2 = 0.5$, $\epsilon_1 = 1.0$, $\epsilon_2 = 2.0$, $\Gamma_1 = 0.20$, and $\Gamma_2 = 0.70$. For $A'_{22}(\omega)$, the parameters are: $f_1 = f_2 = 0.5$, $\epsilon_1 = -1.0$, $\epsilon_2 = -2.1$, $\Gamma_1 = 0.25$, and $\Gamma_2 = 0.60$. The true spectral function is a general matrix with non-zero off-diagonal components. It reads:

$$\mathbf{A}(\omega) = \begin{bmatrix} A_{11}(\omega) & A_{12}(\omega) \\ A_{21}(\omega) & A_{22}(\omega) \end{bmatrix}. \tag{31}$$

The diagonal matrix $\mathbf{A}'(\omega)$ is rotated by a rotation matrix $\mathbf{R}$ to generate $\mathbf{A}(\omega)$. The rotation matrix $\mathbf{R}$ is defined as follows:

$$\mathbf{R} = \begin{bmatrix} \cos\theta & \sin\theta \\ -\sin\theta & \cos\theta \end{bmatrix}, \tag{32}$$

where θ denotes the rotation angle. In the present work, we consider three different rotation angles. They are: (i) $\theta = 0.1$, (ii) $\theta = 0.5$, and (iii) $\theta = 0.9$. Then $\mathbf{A}(\omega)$ is used to construct the matrix-valued Green's function $\mathbf{G}(i\omega_n)$ by using Eq. (4). The essential parameters are: $\delta = 0.0$, $\sigma = 10^{-4}$, and $\beta = 40.0$. The input data contains 50 Matsubara frequencies. For analytic continuations of the diagonal elements of $\mathbf{G}(i\omega_n)$, the default models are Gaussian-like. However, for the off-diagonal elements, the default models are quite different. They are evaluated by $D_{12}(\omega) = \sqrt{A_{11}(\omega)A_{22}(\omega)}$, where $A_{11}(\omega)$ and $A_{22}(\omega)$ are the calculated spectral functions for diagonal elements [55, 60]. This means that we have to carry out analytic continuations for the diagonal elements at first, and then use the diagonal spectra to prepare the default models for the off-diagonal elements. For the MaxEnt-BR method, the preblur algorithm is used to smooth the spectra. The blur parameter is fixed to 0.2.

The simulated results are illustrated in Fig. 3. For the diagonal spectral spectral functions (A_{11} and A_{22}), both the MaxEnt-SJ and MaxEnt-BR methods can accurately resolve the peaks that are close to the Fermi level. However, for the high-energy peaks, the MaxEnt-BR method tends to overestimate their heights and yield sharper peaks [see the peaks around $\omega = 2.0$ in Fig. 3(a), (d), and (g)]. For the off-diagonal spectral functions, only A_{12} is shown, since A_{21} is equivalent to A_{12}. We observe that the major features of A_{12} are well captured by both the MaxEnt-SJ and MaxEnt-BR methods. Undoubtedly, the MaxEnt-SJ method works quite well in all cases. The MaxEnt-BR method exhibits good performance when the rotation angle is small [$\theta = 0.1$, see Fig. 3(c)]. But some wiggles emerge around $\omega = \pm 2.0$ when the rotation angle is large [$\theta = 0.5$ and $\theta = 0.9$, see Fig. 3(f) and (i)]. We test more rotation angles ($0.0 < \theta < 2.0$). It seems that these wiggles won't be enhanced unless the blur parameter b is decreased.

IV. DISCUSSIONS

In previous section, analytic continuations for single-band Green's functions and matrix-valued Green's functions by using the MaxEnt-BR method have been demonstrated. However, there are still some important issues that need to be clar-
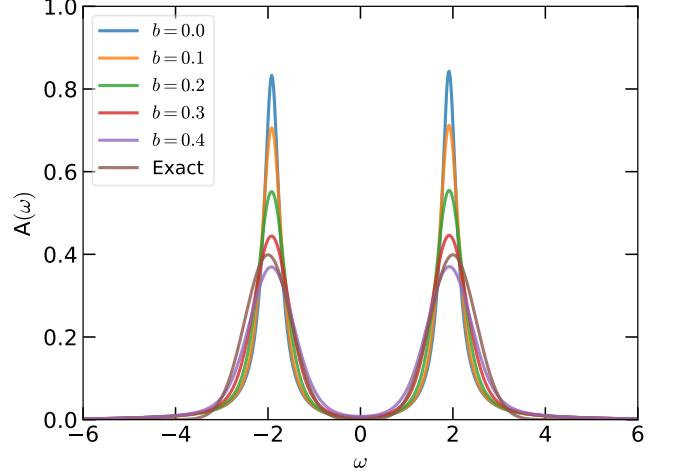

FIG. 4. Test of the preblur trick. A single-band Green's function is treated. The exact spectral function is generated by using Eq. (29). The model parameters are the same as those used in Sec. III B. Only the analytic continuation results obtained by the MaxEnt-BR method are shown.
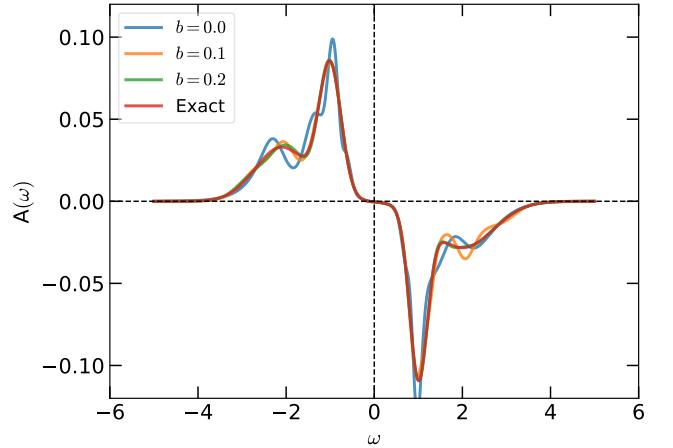

FIG. 5. Test of the preblur trick. A matrix-valued Green's function is treated via the positive-negative entropy approach. The initial spectral function is generated by using Eq. (29). The model parameters are the same as those used in Sec. III C. The rotation angle θ is 0.1. Only the off-diagonal spectral functions (A_{12}) obtained by the MaxEnt-BR method are shown.

ified. In this section, we would like to further discuss the preblur algorithm, the auxiliary Green's algorithm, and the noise tolerance for the MaxEnt-BR method.

A. Effect of preblur

The benchmark results shown in Section III imply that the MaxEnt-BR method has a tendency to generate sharp peaks or small fluctuations in the high-energy regions of the spectra. The preblur algorithm is helpful to alleviate this phenomenon. In the context of analytic continuation, the preblur algorithm
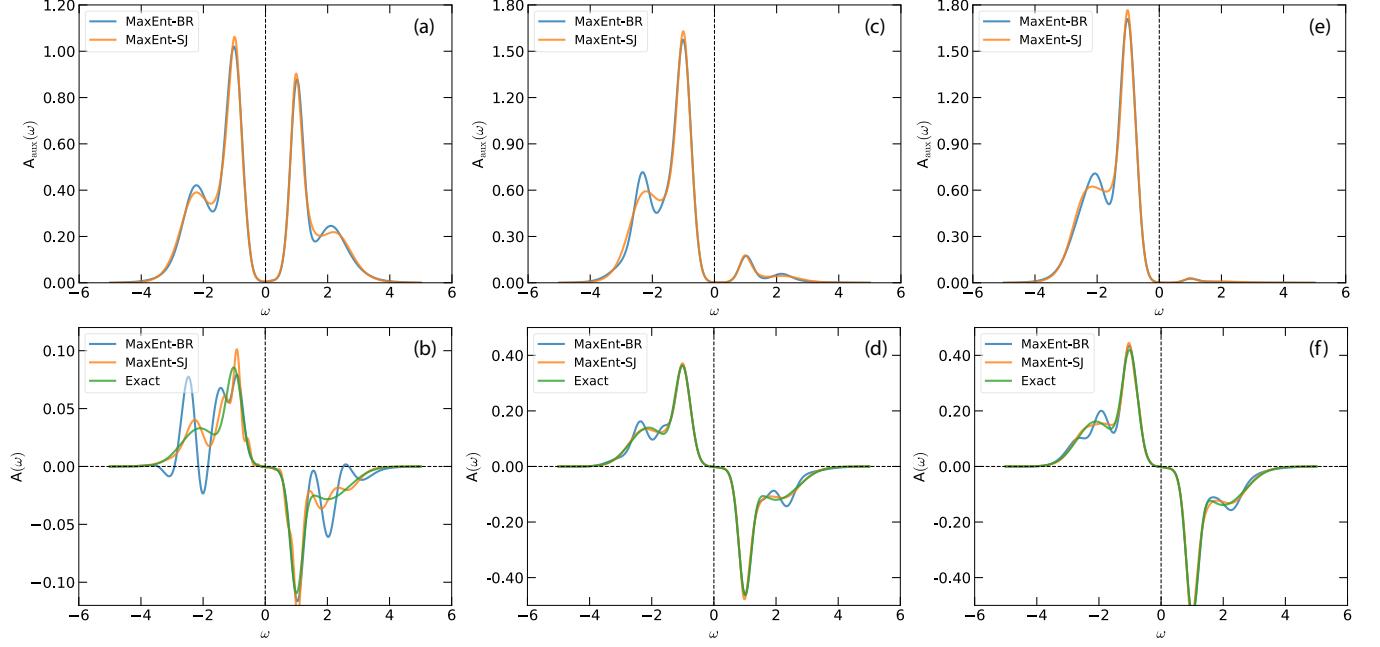
FIG. 6. Analytic continuations of matrix-valued Green's functions via the auxiliary Green's function approach. The model parameters are the same as those used in Sec. III C. For the MaxEnt-BR simulations, the preblur trick is always applied, and the blur parameter b is fixed to 0.2. Only the results for the off-diagonal elements are presented (A_{12}). The upper panels show the spectral functions for the auxiliary Green's functions [see Eq. (35)]. The lower panels show the off-diagonal spectral functions evaluated by Eq. (36). (a)-(b) $\theta = 0.1$; (c)-(d) $\theta = 0.5$; (e)-(f) $\theta = 0.9$.

was introduced by Kraberger *et al.* [55]. The kernel function $K(i\omega_n, \omega)$ [see Eq. (6)] is "blurred" by using the following expression:

$$K_b(i\omega_n, \omega) = \int_{-\infty}^{\infty} d\omega' \, K(i\omega_n, \omega') g_b(\omega - \omega'). \quad (33)$$

Here, $K_b(i\omega_n, \omega)$ is the blurred kernel, which is then used in Eq. (8) to evaluate the χ^2-term. $g_b(\omega)$ is a Gaussian function:

$$g_b(\omega) = \frac{\exp(-\omega^2/2b^2)}{\sqrt{2\pi}b}, \quad (34)$$

where b is the blur parameter.

In Figures 4 and 5, we analyze the effects of the preblur trick for two typical scenarios: (i) Positive spectral function with two separate Gaussian peaks. (ii) Complicated spectral function for off-diagonal Green's function. Note that the model parameters for generating the exact spectra are taken from Sections III B and III C, respectively. It is evident that the MaxEnt-BR method without the preblur trick ($b = 0$) has trouble resolving the spectra accurately. It usually favors sharp peaks (see Fig. 4). Sometimes it may lead to undesirable artifacts, such as the side peaks around $\omega = \pm 1.5$ in Fig. 5. The preblur algorithm can remedy this problem to some extent. The major peaks are smoothed, and the artificial side peaks are suppressed upon increasing b. But it's not the case that bigger is always better. There is an optimal b. For case (i), the optimal b is 0.3. A larger b ($b > 0.3$) will destroy the gap, inducing a metallic state. For case (ii), the optimal b is

0.2. If b is further increased, it is difficult to obtain a stable solution. Here, we should emphasize that these unphysical features seen in the spectra are not unique for the MaxEnt-BR method. Actually, a similar tendency was already observed in the early applications of the MaxEnt-SJ method in image processing tasks. In order to address this problem, Skilling suggested that the spectrum can be expressed as a Gaussian convolution: $A = g_b \star h$, where h is a "hidden" function [79]. Then the entropy is evaluated from $h(\omega)$, instead of $A(\omega)$. In fact, Skilling's approach is equivalent to the preblur trick.

B. Auxiliary Green's functions

As stated before, in addition to the positive-negative entropy method, the auxiliary Green's algorithm can be used to continue the off-diagonal elements of the Green's functions [63–68]. Its idea is quite simple. At first, an auxiliary Green's function is constructed as follows:

$$G_{\text{aux}}(i\omega_n) = G_{11}(i\omega_n) + G_{22}(i\omega_n) + 2G_{12}(i\omega_n). \quad (35)$$

Supposed that $A_{\text{aux}}(\omega)$ is the corresponding spectral function for $G_{\text{aux}}(i\omega_n)$. It is easy to prove that $A_{\text{aux}}(\omega)$ is positive semi-definiteness. So, it is safe to perform analytic continuation for $G_{\text{aux}}(i\omega_n)$ by using the traditional MaxEnt-SJ or MaxEnt-BR method. Next, the off-diagonal spectral function $A_{12}(\omega)$ can be evaluated as follows:

$$A_{12}(\omega) = \frac{A_{\text{aux}}(\omega) - A_{11}(\omega) - A_{22}(\omega)}{2}. \quad (36)$$
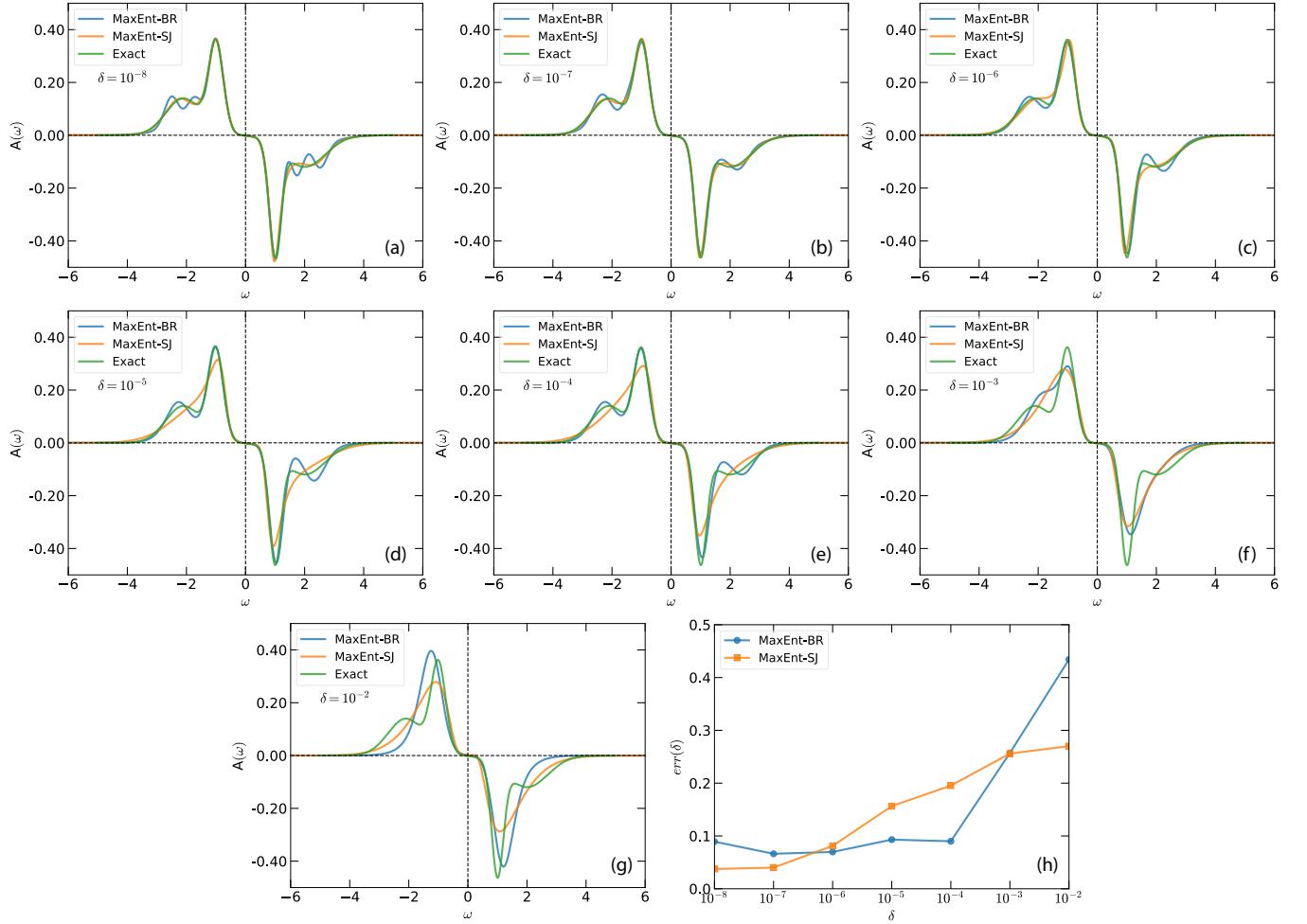
FIG. 7. Robustness of the MaxEnt method with respect to the noisy Matsubara data. Here we treat the off-diagonal elements (G_{12}) of the two-band matrix-valued Green's functions only via the positive-negative entropy method. The model parameters are the same as those used in Sec. III C. The rotation angle θ is 0.5. The blur parameter for the MaxEnt-BR method is fixed to 0.2. (a)-(g) Off-diagonal spectral functions (A_{12}) extracted from noisy Matsubara data. δ denotes the noise level of the input data. It varies from 10^{-8} (tiny noise) to 10^{-2} (large noise). (h) Integrated real axis error as a function of δ. It measures the deviations from the exact spectral function, see Eq. (37).

This algorithm is not restricted to the particle-hole symmetric case, as assumed in Ref. [64]. Here, we employ the two-band's example presented in Section III C again to test the combination of the auxiliary Green's function algorithm and the MaxEnt-BR method (and the MaxEnt-SJ method). The model and computational parameters are kept, and the analytic continuation results are plotted in Fig. 6.

Three rotation angles are considered in the simulations. We find the auxiliary Green's function algorithm is numerically unstable. (i) $\theta = 0.1$. When the rotation angle is small, the amplitude (absolute value) of $A_{12}(\omega)$ is small. Both the MaxEnt-SJ method and the MaxEnt-BR method can resolve the major peaks around $\omega = \pm 1.0$. But they will produce apparent oscillations at higher energies. Increasing the b parameter further could lead to wrong peaks. It seems that these unphysical features are likely due to the superposition of errors in $A_{\text{aux}}(\omega)$, $A_{11}(\omega)$, and $A_{22}(\omega)$. The performance of the MaxEnt-BR method is worse than that of the MaxEnt-SJ method. (ii)

$\theta = 0.5$ and $\theta = 0.9$. When the rotation angle is moderate or large, the spectra obtained by the MaxEnt-SJ method are well consistent with the exact solutions. By using the MaxEnt-BR method, though the fluctuations in high-energy regions are greatly suppressed, small deviations from the exact spectra still exist. Overall, the auxiliary Green's function algorithm is inferior to the positive-negative entropy method in the examples studied. Especially when the rotation angle is small, the auxiliary Green's function algorithm usually fails, irrespective of which form of entropy is adopted.

C. Robustness with respect to noisy input data

Analytic continuation is commonly used on noisy Monte Carlo data. The precision of the Monte Carlo data, which strongly depends on the sampling algorithm and the estimator used, is rarely better than 10^{-5} [3–5]. The distributions

of inherent errors in the Monte Carlo data are often Gaussian. This poses a strict requirement for the noise tolerance of the analytic continuation methods. Previous studies have demonstrated that the MaxEnt-SJ method is robust to noise. Here, we would like to examine the robustness of the MaxEnt-BR method with respect to noisy Matsubara data. We reconsider the analytic continuation of the off-diagonal elements of matrix-valued Green's functions. As mentioned above, the synthetic Matsubara data for this case is assumed to be noiseless ($\delta = 0.0$). Now the noise is manually added by Eq. (26) and the noise level δ is changed from 10^{-8} to 10^{-2}. The other computational parameters are the same as those used in Section III C. In order to estimate the sensitivity of the analytic continuation method to the noisy data, a new quantity, namely integrated real axis error, is introduced:

$$err(\delta) = \int d\omega \, \left| A(\omega) - \hat{A}_\delta(\omega) \right|. \tag{37}$$

Here, $\hat{A}_\delta(\omega)$ means the reconstructed (optimal) spectral function under the given noise level δ.

In Figure 7(a)-(g), the convergence of the spectral functions by the MaxEnt-BR method for simulated Gaussian errors with varying magnitude is shown. When $\delta = 10^{-2}$, the main peaks at $\omega \approx \pm 1.0$ are roughly reproduced, while the side peaks at $\omega \approx 2.0$ are completely smeared out. When $\delta = 10^{-3}$, the major characteristics of the off-diagonal spectrum are successfully captured. As the simulated errors decrease further ($\delta < 10^{-3}$), the MaxEnt-BR method rapidly converges to the exact solution. For comparison, the results for the MaxEnt-SJ method are also presented. It is evident that the MaxEnt-SJ method is less robust than the MaxEnt-BR method when the noise level is moderate. It fails to resolve the satellite peaks around $\omega = \pm 2.0$. Only when $\delta \leq 10^{-6}$, the MaxEnt-SJ method can recover the exact spectrum. Figure 7(h) exhibits the integrated error $err(\delta)$. When $10^{-6} < \delta < 10^{-3}$, the MaxEnt-BR method exhibits better robustness with respect to noise than the MaxEnt-SJ method.

V. CONCLUDING REMARKS

In summary, we extend the application scope of S_{BR} to analytic continuations of imaginary-time Green's functions and Matsubara Green's functions in quantum many-body physics and condense matter physics. It is further generalized to the form of positive-negative entropy to support analytic continuation of matrix-valued Green's function, in which the positive semi-definiteness of the spectral function is broken. We demonstrate that the MaxEnt-BR method, in conjunction with the preblur algorithm and the positive-negative entropy algorithm, is capable of capturing the primary features of the diagonal and off-diagonal spectral functions, even in the presence of moderate levels of noise. Overall, its performance is on par with that of the MaxEnt-SJ method in the examples studied. Possible applications of the MaxEnt-BR method in the future include analytic continuations of anomalous Green's functions and self-energy functions [64, 68], bosonic response

functions (such as optical conductivity and spin susceptibility) [80, 81], and frequency-dependent transport coefficients with non-positive spectral weight [65, 66], etc. Further investigations are highly desirable.

Finally, the MaxEnt-BR method, together with the MaxEnt-SJ method, has been integrated into the open source software package ACFlow [58], which may be useful for the analytic continuation community.

Appendix A: Goodness-of-fit functional

Given the spectral function $A(\omega)$, the Matsubara Green's function $\tilde{G}[A]$ could be reconstructed by using the following equation (the ~ symbol is used to distinguish the reconstructed Green's function from the input Green's function):

$$\tilde{G}_n[A] = \int d\omega \, K(i\omega_n, \omega)A(\omega), \tag{A1}$$

where $K(i\omega_n, \omega)$ denotes the kernel function, and n is the index for Matsubara frequency. For the sake of simplicity, Eq. (A1) is reformulated into its discretization form:

$$\tilde{G}_n[A] = \sum_m K_{nm}A_m\Delta_m, \tag{A2}$$

where $K_{nm} \equiv K(i\omega_n, \omega_m)$, $A_i \equiv A(\omega_i)$, and Δ_i means the weight of the mesh at real axis.

The goodness-of-fit functional $\chi^2[A]$ measures the distance between the input Green's function G and the reconstructed Green's function $\tilde{G}[A]$. Its expression is as follows:

$$\chi^2[A] = \sum_{n=1}^N \frac{(G_n - \tilde{G}_n[A])^2}{\sigma_n^2} \tag{A3}$$

Here we just assume that there are N data points, and σ_n denotes the standard derivative (i.e., the error bar) of G_n. Substituting Eq. (A2) into Eq. (A3), then we arrive:

$$\chi^2[A] = \sum_{n=1}^N \frac{(G_n - \sum_m K_{nm}A_m\Delta_m)^2}{\sigma_n^2}. \tag{A4}$$

The first derivative of $\chi^2[A]$ with respect to A_i reads:

$$\frac{\partial \chi^2[A]}{\partial A_i} = 2 \sum_{n=1}^N \frac{K_{ni}\Delta_i}{\sigma_n^2} \left(\sum_m K_{nm}A_m\Delta_m - G_n \right). \tag{A5}$$

Appendix B: Shannon-Jaynes entropy

In this appendix, the technical details for S_{SJ}, $S_{SJ}^{\pm}$, and the MaxEnt-SJ method are reviewed. Most of the equations presented in this appendix have been derived in Refs. [18], [55], and [60]. We repeat the mathematical derivation here so that this paper is self-contained.

1. Entropy

The Shannon-Jaynes entropy is defined as follows:

$$S_{SJ}[A] = \int d\omega \left[A(\omega) - D(\omega) - A(\omega) \log \left(\frac{A(\omega)}{D(\omega)} \right) \right], \quad \text{(B1)}$$

The discretization form of Eq. (B1) is:

$$S_{SJ}[A] = \sum_i \Delta_i \left[A_i - D_i - A_i \log \left(\frac{A_i}{D_i} \right) \right]. \quad \text{(B2)}$$

The first derivative of $S_{SJ}[A]$ with respect to A_i reads:

$$\frac{\partial S_{SJ}[A]}{\partial A_i} = -\Delta_i \log \left(\frac{A_i}{D_i} \right). \quad \text{(B3)}$$

2. Parameterization of spectral function

A singular value decomposition can be readily performed for the kernel function K:

$$K = U\xi V^T, \quad \text{(B4)}$$

where U and V are column-orthogonal matrices and ξ is the vector of singular values. So, the matrix element of K reads:

$$K_{ni} = \sum_m U_{nm} \xi_m V_{im}. \quad \text{(B5)}$$

The columns of V can be understood as basis functions for the spectral function. That is to say they span a so-called singular value space. And in the singular value space the spectrum can be parameterized through:

$$A_l = D_l \exp \left(\sum_m V_{lm} u_m \right). \quad \text{(B6)}$$

It is easy to prove that:

$$\frac{\partial A_l}{\partial u_i} = D_l \exp \left(\sum_m V_{lm} u_m \right) V_{li} = A_l V_{li}. \quad \text{(B7)}$$

3. Newton's method

Next, we will derive the equations for $\{u_m\}$. Let us recall the stationary condition [see also Eq. (11)]:

$$\frac{\partial Q[A]}{\partial A_i} = 0. \quad \text{(B8)}$$

It is actually:

$$\alpha \frac{\partial S_{SJ}[A]}{\partial A_i} - \frac{1}{2} \frac{\partial \chi^2[A]}{\partial A_i} = 0. \quad \text{(B9)}$$

Substituting Eqs. (B3) and (A5) into the above equation:

$$\alpha \Delta_i \log \left(\frac{A_i}{D_i} \right) + \sum_{n=1}^N \frac{K_{ni} \Delta_i}{\sigma_n^2} \left(\sum_m K_{nm} A_m \Delta_m - G_n \right) = 0. \quad \text{(B10)}$$

Eliminating Δ_i:

$$\alpha \log \left(\frac{A_i}{D_i} \right) + \sum_{n=1}^N \frac{K_{ni}}{\sigma_n^2} \left(\sum_m K_{nm} A_m \Delta_m - G_n \right) = 0. \quad \text{(B11)}$$

Substituting Eqs. (B6) and (B5) into Eq. (B11):

$$\alpha \sum_m V_{im} u_m +$$
$$\sum_{n=1}^N \frac{1}{\sigma_n^2} \sum_m U_{nm} \xi_m V_{im} \left(\sum_l K_{nl} A_l \Delta_l - G_n \right) = 0 \quad \text{(B12)}$$

Now $\sum_m V_{im}$ can be removed from the two terms in the left-hand side. Finally we get:

$$\alpha u_m + \sum_{n=1}^N \frac{1}{\sigma_n^2} \xi_m U_{nm} \left(\sum_l K_{nl} A_l \Delta_l - G_n \right) = 0. \quad \text{(B13)}$$

Since A_l depends on $\{u_m\}$ as well, Eq. (B13) is actually a nonlinear equation about $\{u_m\}$. In the ACFlow package [58], the Newton's method is adopted to solve it. So we have to evaluate the following two variables and pass them to the Newton's algorithm [75]:

$$f_m = \alpha u_m + \xi_m \sum_{n=1}^N \frac{1}{\sigma_n^2} U_{nm} \left(\sum_l K_{nl} A_l \Delta_l - G_n \right), \quad \text{(B14)}$$

$$J_{mi} = \frac{\partial f_m}{\partial u_i} = \alpha \delta_{mi} + \xi_m \sum_{n=1}^N \frac{1}{\sigma_n^2} U_{nm} \sum_l K_{nl} A_l \Delta_l V_{li}, \quad \text{(B15)}$$

where J_{mi} can be considered as a Jacobian matrix. Note that Eq. (B7) is applied to derive Eq. (B15).

Since the calculations for f_m and J_{mi} are quite complicated and time-consuming, the Einstein summation technology is used to improve the computational efficiency. The following three variables should be precomputed and stored during the initialization stage:

$$B_m = \sum_{n=1}^N \frac{1}{\sigma_n^2} \xi_m U_{nm} G_n, \quad \text{(B16)}$$

$$W_{ml} = \sum_{pn} \frac{1}{\sigma_n^2} U_{nm} \xi_m U_{np} \xi_p V_{lp} \Delta_l D_l, \quad \text{(B17)}$$

$$W_{mli} = W_{ml} V_{li}. \quad \text{(B18)}$$

Clearly, the three variables only depend on the input Green's function G, the default model D, and the singular value decomposition of the kernel function K. Now f_m and J_{mi} can be reformulated in terms of them:

$$f_m = \alpha u_m + \sum_l W_{ml} w_l - B_m, \tag{B19}$$

$$J_{mi} = \alpha \delta_{mi} + \sum_l W_{mli} w_l, \tag{B20}$$

where

$$w_l = \exp\left(\sum_m V_{lm} u_m\right). \tag{B21}$$

4. Positive-negative entropy

For matrix-valued Green's function, the spectral functions of the off-diagonal components could exhibit negative weight.

However, the ordinary MaxEnt method is only rigorous for non-negative spectrum [18]. In order to remedy this problem, one could imagine that the off-diagonal spectral functions originate from a subtraction of two artificial positive functions [55],

$$A = A^+ - A^-, \tag{B22}$$

$$A^- = A^+ - A. \tag{B23}$$

Assuming the independence of A^+ and A^-, the resulting entropy $S_{SJ}[A^+, A^-]$ is the sum of the respective entropies:

$$S_{SJ}[A^+, A^-] = \int d\omega \left[A^+ - D - A^+ \log\left(\frac{A^+}{D}\right) \right] + \int d\omega \left[A^- - D - A^- \log\left(\frac{A^-}{D}\right) \right]. \tag{B24}$$

Thus, $S_{SJ}[A^+, A^-]$ is called the positive-negative entropy in the literature [55, 60]. We at first eliminate A^-

$$S_{SJ}[A, A^+] = \int d\omega \left[A^+ - D - A^+ \log\left(\frac{A^+}{D}\right) \right] + \int d\omega \left[(A^+ - A) - D - (A^+ - A) \log\left(\frac{A^+ - A}{D}\right) \right], \tag{B25}$$

and write:

$$Q[A, A^+] = \alpha S_{SJ}[A, A^+] - \frac{1}{2}\chi^2[A]. \tag{B26}$$

Since we are searching for a maximum of Q with respect to A and A^+, we also apply:

$$\frac{\partial Q[A, A^+]}{\partial A^+} = \frac{\partial S_{SJ}[A, A^+]}{\partial A^+} = 0, \tag{B27}$$

to eliminate A^+. The following equations show some intermediate steps:

$$\int d\omega \left[\log\left(\frac{A^+}{D}\right) + \log\left(\frac{A^+ - A}{D}\right) \right] = 0, \tag{B28}$$

$$\log\left(\frac{A^+}{D}\right) + \log\left(\frac{A^+ - A}{D}\right) = 0, \tag{B29}$$

$$\frac{A^+(A^+ - A)}{D^2} = 1. \tag{B30}$$

Finally, we obtain:

$$A^+ = \frac{\sqrt{A^2 + 4D^2} + A}{2}, \tag{B31}$$

$$A^- = \frac{\sqrt{A^2 + 4D^2} - A}{2}. \tag{B32}$$

Substituting Eqs. (B31) and (B32) into Eq. (B24) to eliminate A^+ and A^-, we obtain:

$$S_{SJ}[A^+, A^-] = \int d\omega \left[\sqrt{A^2 + 4D^2} - 2D - A \log\left(\frac{\sqrt{A^2 + 4D^2} + A}{2D}\right) \right]. \tag{B33}$$

Its discretization form becomes:

$$S_{SJ}[A^+, A^-] = \sum_m \left[\sqrt{A_m^2 + 4D_m^2} - 2D_m - A_m \log\left(\frac{\sqrt{A_m^2 + 4D_m^2} + A_m}{2D_m}\right) \right] \Delta_m. \tag{B34}$$

Note that Eq. (B33) is exactly the same with Eq. (19). $S_{SJ}[A^+, A^-]$ is just $S_{SJ}^{\pm}[A]$. The first derivative of $S_{SJ}[A^+, A^-]$ with respect to A_i is:

$$\frac{\partial S_{SJ}[A^+, A^-]}{\partial A_i} = -\Delta_i \log\left(\frac{A_i^+}{D_i}\right). \tag{B35}$$

5. Parameterization for positive-negative spectral functions

According to Eq. (B31) and Eq. (B32), we find:

$$A^+ A^- = D^2. \tag{B36}$$

Inspired by Eq. (B6), it is naturally to parameterize A^+ and A^- in the singular value space as well:

$$A_i^+ = D_i \exp\left(\sum_m V_{im} u_m\right), \tag{B37}$$

$$A_i^- = D_i \exp\left(-\sum_m V_{im} u_m\right). \tag{B38}$$

Hence,

$$A_i = D_i \exp\left(\sum_m V_{im} u_m\right) - D_i \exp\left(-\sum_m V_{im} u_m\right) \tag{B39}$$

$$A_i = D_i \left(w_i - \frac{1}{w_i}\right). \tag{B40}$$

$$\frac{\partial A_l^+}{\partial u_i} = A_l^+ V_{li}. \tag{B41}$$

$$\frac{\partial A_l^-}{\partial u_i} = -A_l^- V_{li}. \tag{B42}$$

$$\frac{\partial A}{\partial u_i} = (A_l^+ + A_l^-) V_{li} = D_l \left(w_l + \frac{1}{w_l}\right) V_{li}. \tag{B43}$$

By using the Einstein summation notations as defined in Section B 3, we immediately obtain:

$$f_m = \alpha u_m + \sum_l W_{ml}\left(w_l - \frac{1}{w_l}\right) - B_m, \tag{B44}$$

$$J_{mi} = \alpha \delta_{mi} + \sum_l W_{mli}\left(w_l + \frac{1}{w_l}\right). \tag{B45}$$

Appendix C: Bayesian reconstruction entropy

In this appendix, the technical details for S_{BR}, $S_{\mathrm{BR}}^{\pm}$, and the MaxEnt-BR method are discussed.

1. Entropy

The Bayesian reconstruction entropy reads:

$$S_{\mathrm{BR}}[A] = \int d\omega \left[1 - \frac{A(\omega)}{D(\omega)} + \log\left(\frac{A(\omega)}{D(\omega)}\right)\right]. \tag{C1}$$

Its discretization form is:

$$S_{\mathrm{BR}}[A] = \sum_i \Delta_i \left[1 - \frac{A_i}{D_i} + \log\left(\frac{A_i}{D_i}\right)\right]. \tag{C2}$$

Its first derivative with respect to A_i is:

$$\frac{\partial S_{\mathrm{BR}}[A]}{\partial A_i} = -\Delta_i \left(\frac{1}{D_i} - \frac{1}{A_i}\right). \tag{C3}$$

2. Parameterization of spectral function

The original parameterization of A [see Eq. (B6)] can not be used here. A new parameterization scheme for A is necessary. Assumed that

$$\frac{1}{D_i} - \frac{1}{A_i} = \sum_m V_{im} u_m, \tag{C4}$$

then we have:

$$A_l = \frac{D_l}{1 - D_l \sum_m V_{lm} u_m}. \tag{C5}$$

So, the first derivative of A_l with respect to u_i reads:

$$\frac{\partial A_l}{\partial u_i} = A_l A_l V_{li}. \tag{C6}$$

3. Newton's method

Next, we would like to derive f_m and J_{mi} for the Bayesian reconstruction entropy. Substituting Eq. (C3) into Eq. (B9):

$$\alpha \Delta_i \left(\frac{1}{D_i} - \frac{1}{A_i}\right) + \sum_{n=1}^N \frac{K_{ni}\Delta_i}{\sigma_n^2}\left(\sum_m K_{nm} A_m \Delta_m - G_n\right) = 0. \tag{C7}$$

Eliminating Δ_i:

$$\alpha\left(\frac{1}{D_i} - \frac{1}{A_i}\right) + \sum_{n=1}^N \frac{K_{ni}}{\sigma_n^2}\left(\sum_m K_{nm} A_m \Delta_m - G_n\right) = 0. \tag{C8}$$

Substituting Eq. (C4) into Eq. (C8):

$$\alpha \sum_m V_{im} u_m + $$
$$\sum_{n=1}^N \frac{1}{\sigma_n^2}\sum_m U_{nm}\xi_m V_{im}\left(\sum_l K_{nl} A_l \Delta_l - G_n\right) = 0. \tag{C9}$$

Eliminating $\sum_m V_{im}$ again:

$$\alpha u_m + \sum_{n=1}^N \frac{1}{\sigma_n^2}\xi_m U_{nm}\left(\sum_l K_{nl} A_l \Delta_l - G_n\right) = 0. \tag{C10}$$

Clearly, Eq. (C10) is the same with Eq. (B13). Thus, the equations for f_m and J_{mi} are as follows:

$$f_m = \alpha u_m + \xi_m \sum_{n=1}^N \frac{1}{\sigma_n^2} U_{nm}\left(\sum_l K_{nl} A_l \Delta_l - G_n\right), \tag{C11}$$

$$J_{mi} = \frac{\partial f_m}{\partial u_i} = \alpha \delta_{mi} + \xi_m \sum_{n=1}^N \frac{1}{\sigma_n^2} U_{nm} \sum_l K_{nl} A_l A_l \Delta_l V_{li}. \tag{C12}$$

Note that Eq. (C11) is the same with Eq. (B14). However, Eq. (C12) differs from Eq. (B15) by a factor A_l in the second term of the right-hand side. To derive Eq. (C12), Eq. (C6)

is used. Now the Einstein summation notation is adopted to simplify the calculations of f_m and J_{mi} again:

$$f_m = \alpha u_m + \sum_l W_{ml} w_l - B_m, \tag{C13}$$

$$J_{mi} = \alpha \delta_{mi} + \sum_l W_{mli} D_l w_l w_l, \tag{C14}$$

where

$$w_l = \frac{1}{1 - D_l \sum_m V_{lm} u_m}. \tag{C15}$$

Here, the definitions of W_{ml}, W_{mli}, and B_m could be found in Section B 3.

4. Positive-negative entropy

Next, we would like to generalize the Bayesian reconstruction entropy to realize the positive-negative entropy algorithm to support the analytic continuation of matrix-valued Green's function [55]. The positive-negative entropy for the Bayesian reconstruction entropy is defined as follows:

$$S_{BR}[A^+, A^-] = \int d\omega \left[1 - \frac{A^+}{D} + \log\left(\frac{A^+}{D}\right) \right]$$

$$+ \int d\omega \left[1 - \frac{A^-}{D} + \log\left(\frac{A^-}{D}\right) \right]. \tag{C16}$$

Since $A = A^+ - A^-$, Eq. (C16) can be transformed into:

$$S_{BR}[A, A^+] = \int d\omega \left[1 - \frac{A^+}{D} + \log\left(\frac{A^+}{D}\right) \right]$$

$$+ \int d\omega \left[1 - \frac{A^+ - A}{D} + \log\left(\frac{A^+ - A}{D}\right) \right] \tag{C17}$$

Then we should eliminate A^+ in Eq. (C17). Because

$$\frac{\partial S_{BR}[A, A^+]}{\partial A^+} = 0 = \int d\omega \left(\frac{1}{A^+} + \frac{1}{A^+ - A} - \frac{2}{D} \right), \tag{C18}$$

we immediately get:

$$A^+ = \frac{\sqrt{A^2 + D^2} + D + A}{2}, \tag{C19}$$

and

$$A^- = \frac{\sqrt{A^2 + D^2} + D - A}{2}. \tag{C20}$$

From the definitions of A^+ and A^-, it is easily to prove:

$$2A^+ A^- = (A^+ + A^-)D, \tag{C21}$$

and

$$A^+ + A^- = \sqrt{A^2 + D^2} + D. \tag{C22}$$

We would like to express $S_{BR}[A^+, A^-]$ in terms of A:

$$S_{BR}[A^+, A^-] = \int d\omega \left[2 - \frac{A^+}{D} - \frac{A^-}{D} + \log\left(\frac{A^+ A^-}{D^2}\right) \right]. \tag{C23}$$

Substituting Eq. (C21) into Eq. (C23):

$$S_{BR}[A^+, A^-] = \int d\omega \left[2 - \frac{A^+ + A^-}{D} + \log\left(\frac{A^+ + A^-}{2D}\right) \right]. \tag{C24}$$

Substituting Eq. (C22) into Eq. (C24):

$$S_{BR}[A^+, A^-] = \int d\omega \left[2 - \frac{\sqrt{A^2 + D^2} + D}{D} + \log\left(\frac{\sqrt{A^2 + D^2} + D}{2D}\right) \right]. \tag{C25}$$

Its discretization form reads:

$$S_{BR}[A^+, A^-] = \sum_m \left[2 - \frac{\sqrt{A_m^2 + D_m^2} + D_m}{D_m} + \log\left(\frac{\sqrt{A_m^2 + D_m^2} + D_m}{2D_m}\right) \right] \Delta_m. \tag{C26}$$

Note that Eq. (C25) is exactly the same with Eq. (20). $S_{BR}[A^+, A^-]$ is just $S_{BR}^{\pm}[A]$. Then the first derivative of $S_{BR}[A^+, A^-]$ with respect to A_i is:

$$\frac{\partial S[A^+, A^-]}{\partial A_i} = -\Delta_i \left(\frac{1}{D_i} - \frac{1}{A_i^+} \right) \tag{C27}$$

This equation is very similar to Eq. (C3).

5. Parameterization for positive-negative spectral functions

Now we assume that:

$$A_l^+ = \frac{D_l}{1 - D_l \sum_m V_{lm} u_m}, \tag{C28}$$

and

$$A_l^- = \frac{D_l}{1 + D_l \sum_m V_{lm} u_m}. \tag{C29}$$

We also introduce:

$$w_l^+ = \frac{1}{1 - D_l \sum_m V_{lm} u_m}, \tag{C30}$$

and

$$w_l^- = \frac{1}{1 + D_l \sum_m V_{lm} u_m}. \tag{C31}$$

So $A_l^+ = D_l w_l^+$, $A_l^- = D_l w_l^-$, and $A_l = D_l(w_l^+ - w_l^-)$. It is easy to verify that the definitions of A_l^+ and A_l^- obey Eq. (C21). The first derivatives of A_l^+ and A_l^- with respect to u_i are:

$$\frac{\partial A_l^+}{\partial u_i} = A_l^+ A_l^+ V_{li}, \tag{C32}$$

and

$$\frac{\partial A_l^-}{\partial u_i} = -A_l^- A_l^- V_{li}. \tag{C33}$$

The first derivative of A_l with respect to u_i is:

$$\frac{\partial A_l}{\partial u_i} = A_l^+ A_l^+ V_{li} + A_l^- A_l^- V_{li}. \tag{C34}$$

After some simple algebra, we easily get:

$$f_m = \alpha u_m + \sum_l W_{ml}(w_l^+ - w_l^-) - B_m, \tag{C35}$$

$$J_{mi} = \alpha \delta_{mi} + \sum_l W_{mli} D_l(w_l^+ w_l^+ + w_l^- w_l^-). \tag{C36}$$

[1] John W. Negele and Henri Orland, *Quantum Many-Particle Systems* (Perseus Books, 1998).

[2] Piers Coleman, *Introduction to Many-Body Physics* (Cambridge University Press, 2016).

[3] Emanuel Gull, Andrew J. Millis, Alexander I. Lichtenstein, Alexey N. Rubtsov, Matthias Troyer, and Philipp Werner, "Continuous-time Monte Carlo methods for quantum impurity models," Rev. Mod. Phys. **83**, 349–404 (2011).

[4] W. M. C. Foulkes, L. Mitas, R. J. Needs, and G. Rajagopal, "Quantum Monte Carlo simulations of solids," Rev. Mod. Phys. **73**, 33–83 (2001).

[5] James Gubernatis, Naoki Kawashima, and Philipp Werner, *Quantum Monte Carlo Methods: Algorithms for Lattice Models* (Cambridge University Press, 2016).

[6] Walter Metzner, Manfred Salmhofer, Carsten Honerkamp, Volker Meden, and Kurt Schönhammer, "Functional renormalization group approach to correlated fermion systems," Rev. Mod. Phys. **84**, 299–352 (2012).

[7] W. Hanke C. Platt and R. Thomale, "Functional renormalization group for multi-orbital Fermi surface instabilities," Adv. Phys. **62**, 453–562 (2013).

[8] Judith Harl and Georg Kresse, "Accurate Bulk Properties from Approximate Many-Body Techniques," Phys. Rev. Lett. **103**, 056401 (2009).

[9] Guo P. Chen, Vamsee K. Voora, Matthew M. Agee, Sree Ganesh Balasubramani, and Filipp Furche, "Random-Phase Approximation Methods," Annu. Rev. Phys. Chem. **68**, 421–445 (2017).

[10] Lars Hedin, "New Method for Calculating the One-Particle Green's Function with Application to the Electron-Gas Problem," Phys. Rev. **139**, A796–A823 (1965).

[11] F Aryasetiawan and O Gunnarsson, "The GW method," Rep. Prog. Phys. **61**, 237 (1998).

[12] Giovanni Onida, Lucia Reining, and Angel Rubio, "Electronic excitations: density-functional versus many-body Green's-function approaches," Rev. Mod. Phys. **74**, 601–659 (2002).

[13] Jan Gukelberger, Li Huang, and Philipp Werner, "On the dangers of partial diagrammatic summations: Benchmarks for the two-dimensional Hubbard model in the weak-coupling regime," Phys. Rev. B **91**, 235114 (2015).

[14] K. S. D. Beach, R. J. Gooding, and F. Marsiglio, "Reliable Padé analytical continuation method based on a high-accuracy symbolic computation algorithm," Phys. Rev. B **61**, 5147–5157 (2000).

[15] Johan Schött, Inka L. M. Locht, Elin Lundin, Oscar Grånäs, Olle Eriksson, and Igor Di Marco, "Analytic continuation by averaging Padé approximants," Phys. Rev. B **93**, 075104 (2016).

[16] H. J. Vidberg and J. W. Serene, "Solving the Eliashberg equations by means of N-point Padé approximants," J. Low Temp. Phys. **29**, 179–192 (1977).

[17] Gergely Markó, Urko Reinosa, and Zsolt Szép, "Padé approximants and analytic continuation of Euclidean Φ-derivable approximations," Phys. Rev. D **96**, 036002 (2017).

[18] Mark Jarrell and J.E. Gubernatis, "Bayesian inference and the analytic continuation of imaginary-time quantum Monte Carlo data," Phys. Rep. **269**, 133–195 (1996).

[19] J. E. Gubernatis, Mark Jarrell, R. N. Silver, and D. S. Sivia, "Quantum Monte Carlo simulations and maximum entropy: Dynamics from imaginary-time data," Phys. Rev. B **44**, 6011–6029 (1991).

[20] R. N. Silver, D. S. Sivia, and J. E. Gubernatis, "Maximum-entropy method for analytic continuation of quantum Monte Carlo data," Phys. Rev. B **41**, 2380–2389 (1990).

[21] Anders W. Sandvik, "Stochastic method for analytic continuation of quantum Monte Carlo data," Phys. Rev. B **57**, 10287–10290 (1998).

[22] Anders W. Sandvik, "Constrained sampling method for analytic continuation," Phys. Rev. E **94**, 063308 (2016).

[23] Hui Shao and Anders W. Sandvik, "Progress on stochastic analytic continuation of quantum Monte Carlo data," Phys. Rep. **1003**, 1–88 (2023).

[24] K. S. D. Beach, "Identifying the maximum entropy method as a special limit of stochastic analytic continuation," (2004), arXiv:0403055 [cond-mat.str-el].

[25] Sebastian Fuchs, Thomas Pruschke, and Mark Jarrell, "Analytic continuation of quantum Monte Carlo data by stochastic analytical inference," Phys. Rev. E **81**, 056701 (2010).

[26] K. Vafayi and O. Gunnarsson, "Analytical continuation of spectral data from imaginary time axis to real frequency axis using statistical sampling," Phys. Rev. B **76**, 035115 (2007).

[27] David R. Reichman and Eran Rabani, "Analytic continuation average spectrum method for quantum liquids," J. Chem. Phys. **131**, 054502 (2009).

[28] Khaldoon Ghanem and Erik Koch, "Extending the average spectrum method: Grid point sampling and density averaging," Phys. Rev. B **102**, 035114 (2020).

[29] Khaldoon Ghanem and Erik Koch, "Average spectrum method for analytic continuation: Efficient blocked-mode sampling and dependence on the discretization grid," Phys. Rev. B **101**, 085111 (2020).

[30] Olav F. Syljuåsen, "Using the average spectrum method to extract dynamics from quantum Monte Carlo simulations," Phys. Rev. B **78**, 174429 (2008).

[31] A. S. Mishchenko, N. V. Prokof'ev, A. Sakamoto, and B. V. Svistunov, "Diagrammatic quantum Monte Carlo study of the Fröhlich polaron," Phys. Rev. B **62**, 6317–6336 (2000).

[32] F. Bao, Y. Tang, M. Summers, G. Zhang, C. Webster, V. Scarola, and T. A. Maier, "Fast and efficient stochastic optimization for analytic continuation," Phys. Rev. B **94**, 125149 (2016).

[33] Olga Goulko, Andrey S. Mishchenko, Lode Pollet, Nikolay Prokof'ev, and Boris Svistunov, "Numerical analytic continuation: Answers to well-posed questions," Phys. Rev. B **95**, 014102 (2017).

[34] Igor Krivenko and Malte Harland, "TRIQS/SOM: Implementation of the stochastic optimization method for analytic continuation," Comput. Phys. Commun. **239**, 166–183 (2019).

[35] Igor Krivenko and Andrey S. Mishchenko, "TRIQS/SOM 2.0: Implementation of the stochastic optimization with consistent constraints for analytic continuation," Comput. Phys. Commun. **280**, 108491 (2022).

[36] Li Huang and Shuang Liang, "Stochastic pole expansion method for analytic continuation of the Green's function," Phys. Rev. B **108**, 235143 (2023).

[37] Li Huang and Shuang Liang, "Reconstructing lattice QCD spectral functions with stochastic pole expansion and Nevanlinna analytic continuation," (2023), arXiv:2309.11114 [hep-lat].

[38] Junya Otsuki, Masayuki Ohzeki, Hiroshi Shinaoka, and Kazuyoshi Yoshimi, "Sparse modeling approach to analytical continuation of imaginary-time quantum monte carlo data," Phys. Rev. E **95**, 061302 (2017).

[39] Yuichi Motoyama, Kazuyoshi Yoshimi, and Junya Otsuki, "Robust analytic continuation combining the advantages of the sparse modeling approach and the padé approximation," Phys. Rev. B **105**, 035139 (2022).

[40] Jiani Fei, Chia-Nan Yeh, and Emanuel Gull, "Nevanlinna Analytical Continuation," Phys. Rev. Lett. **126**, 056402 (2021).

[41] Jiani Fei, Chia-Nan Yeh, Dominika Zgid, and Emanuel Gull, "Analytical continuation of matrix-valued functions: Carathéodory formalism," Phys. Rev. B **104**, 165111 (2021).

[42] Zhen Huang, Emanuel Gull, and Lin Lin, "Robust analytic continuation of Green's functions via projection, pole estimation, and semidefinite relaxation," Phys. Rev. B **107**, 075151 (2023).

[43] Lei Zhang and Emanuel Gull, "Minimal Pole Representation and Controlled Analytic Continuation of Matsubara Response Functions," (2023), arXiv:2312.10576 [cond-mat.str-el].

[44] Lexing Ying, "Pole Recovery From Noisy Data on Imaginary Axis," J. Sci. Comput. **92**, 107 (2022).

[45] Lexing Ying, "Analytic continuation from limited noisy Matsubara data," J. Comput. Phys. **469**, 111549 (2022).

[46] Romain Fournier, Lei Wang, Oleg V. Yazyev, and QuanSheng Wu, "Artificial Neural Network Approach to the Analytic Continuation Problem," Phys. Rev. Lett. **124**, 056401 (2020).

[47] Hongkee Yoon, Jae-Hoon Sim, and Myung Joon Han, "Analytic continuation via domain knowledge free machine learning," Phys. Rev. B **98**, 245101 (2018).

[48] Dongchen Huang and Yi-feng Yang, "Learned optimizers for analytic continuation," Phys. Rev. B **105**, 075112 (2022).

[49] Rong Zhang, Maximilian E. Merkel, Sophie Beck, and Claude Ederer, "Training biases in machine learning for the analytic continuation of quantum many-body Green's functions," Phys. Rev. Res. **4**, 043082 (2022).

[50] Juan Yao, Ce Wang, Zhiyuan Yao, and Hui Zhai, "Noise enhanced neural networks for analytic continuation," Mach. Learn.: Sci. Technol. **3**, 025010 (2022).

[51] Louis-François Arsenault, Richard Neuberg, Lauren A Hannah, and Andrew J Millis, "Projected regression method for solving Fredholm integral equations arising in the analytic continuation problem of quantum physics," Inv. Prob. **33**, 115007 (2017).

[52] Nathan S. Nichols, Paul Sokol, and Adrian Del Maestro, "Parameter-free differential evolution algorithm for the analytic continuation of imaginary time correlation functions," Phys. Rev. E **106**, 025312 (2022).

[53] Dominic Bergeron and A.-M. S. Tremblay, "Algorithms for optimized maximum entropy and diagnostic tools for analytic continuation," Phys. Rev. E **94**, 023303 (2016).

[54] Jae-Hoon Sim and Myung Joon Han, "Maximum quantum entropy method," Phys. Rev. B **98**, 205102 (2018).

[55] Gernot J. Kraberger, Robert Triebl, Manuel Zingl, and Markus Aichhorn, "Maximum entropy formalism for the analytic continuation of matrix-valued Green's functions," Phys. Rev. B **96**, 155128 (2017).

[56] Ryan Levy, J.P.F. LeBlanc, and Emanuel Gull, "Implementation of the maximum entropy method for analytic continuation," Comput. Phys. Commun. **215**, 149–155 (2017).

[57] F. F. Assaad, M. Bercx, F. Goth, A. Götz, J. S. Hofmann, E. Huffman, Z. Liu, F. Parisen Toldin, J. S. E. Portela, and J. Schwab, "The ALF (Algorithms for Lattice Fermions) project release 2.0. Documentation for the auxiliary-field quantum Monte Carlo code," SciPost Phys. Codebases , 1 (2022).

[58] Li Huang, "ACFlow: An open source toolkit for analytic continuation of quantum Monte Carlo data," Comput. Phys. Commun. **292**, 108863 (2023).

[59] Kristjan Haule, Chuck-Hou Yee, and Kyoo Kim, "Dynamical mean-field theory within the full-potential methods: Electronic structure of $CeIrIn_5$, $CeCoIn_5$, and $CeRhIn_5$," Phys. Rev. B **81**, 195107 (2010).

[60] Josef Kaufmann and Karsten Held, "ana_cont: Python package for analytic continuation," Comput. Phys. Commun. **282**, 108519 (2023).

[61] Athanasios Papoulis, *Probability and Statistics* (Prentice Hall, 1989).

[62] M. De Raychaudhury, E. Pavarini, and O. K. Andersen, "Orbital Fluctuations in the Different Phases of $LaVO_3$ and YVO_3,"

Phys. Rev. Lett. **99**, 126402 (2007).

[63] Jan M. Tomczak and Silke Biermann, "Effective band structure of correlated materials: the case of VO$_2$," J. Phys.: Condens. Matter **19**, 365206 (2007).

[64] E. Gull and A. J. Millis, "Pairing glue in the two-dimensional Hubbard model," Phys. Rev. B **90**, 041110 (2014).

[65] A. Reymbaut, D. Bergeron, and A.-M. S. Tremblay, "Maximum entropy analytic continuation for spectral functions with nonpositive spectral weight," Phys. Rev. B **92**, 060509 (2015).

[66] A. Reymbaut, A.-M. Gagnon, D. Bergeron, and A.-M. S. Tremblay, "Maximum entropy analytic continuation for frequency-dependent transport coefficients with nonpositive spectral weight," Phys. Rev. B **95**, 121104 (2017).

[67] Emanuel Gull, Olivier Parcollet, and Andrew J. Millis, "Superconductivity and the Pseudogap in the Two-Dimensional Hubbard Model," Phys. Rev. Lett. **110**, 216405 (2013).

[68] Changming Yue and Philipp Werner, "Maximum entropy analytic continuation of anomalous self-energies," (2023), arXiv:2303.16888 [cond-mat.supr-con].

[69] E. T. Jaynes, "Information Theory and Statistical Mechanics," Phys. Rev. **106**, 620–630 (1957).

[70] A. N. Tikhonov, A. V. Goncharsky, V. V. Stepanov, and A. G. Yagola, *Numerical Methods for the Solution of Ill-Posed Problems* (Springer Netherlands, 1995).

[71] M. Asakawa, Y. Nakahara, and T. Hatsuda, "Maximum entropy analysis of the spectral functions in lattice QCD," Prog. Part. Nucl. Phys. **46**, 459–508 (2001).

[72] Yannis Burnier and Alexander Rothkopf, "Bayesian Approach to Spectral Function Reconstruction for Euclidean Quantum Field Theories," Phys. Rev. Lett. **111**, 182003 (2013).

[73] Alexander Rothkopf, "Bayesian inference of real-time dynamics from lattice QCD," Front. Phys. **10**, 1028995 (2022).

[74] Alexander Rothkopf, "Bayesian inference of nonpositive spectral functions in quantum field theory," Phys. Rev. D **95**, 056016 (2017).

[75] Jorge Nocedal and Stephen J. Wright, *Numerical Optimization* (Springer New York, NY, 2006).

[76] E. D. Laue, J. Skilling, and J. Staunton, "Maximum entropy reconstruction of spectra containing antiphase peaks," J. Magn. Reson. **63**, 418–424 (1985).

[77] Sibusiso Sibisi, "Quantified Maxent: An NMR Application," in *Maximum Entropy and Bayesian Methods*, edited by Paul F. Fougère (Springer Netherlands, Dordrecht, 1990) pp. 351–358.

[78] R. K. Bryan, "Maximum entropy analysis of oversampled data problems," Eur. Biophys. J. **18**, 165–174 (1990).

[79] J Skilling, "Fundamentals of MaxEnt in data analysis," in *Maximum Entropy in Action: A Collection Of Expository Essays* (Oxford University Press, 1991).

[80] O. Gunnarsson, M. W. Haverkort, and G. Sangiovanni, "Analytical continuation of imaginary axis data for optical conductivity," Phys. Rev. B **82**, 165125 (2010).

[81] J. Schött, E. G. C. P. van Loon, I. L. M. Locht, M. I. Katsnelson, and I. Di Marco, "Comparison between methods of analytical continuation for bosonic functions," Phys. Rev. B **94**, 245140 (2016).